A Lightweight Lateral Inhibition Network for Single MR Image Super-Resolution

Xiaole Zhao[1], Tao Zhang[1], and Xueming Zou[1]

School of Life Science and Technology, UESTC, Chengdu 611731, China
`zxlation@foxmail.com; taozhangjin@gmail.com; mark.zou@alltechmed.com`

Abstract. In recent years, convolutional neural networks (CNNs) have shown their advantages on single MR image super-resolution tasks. Many current SR models, however, have heavy demands on computation and memory, which are not friendly to magnetic resonance imaging (MRI) where computing resource is usually limited. On the other hand, a basic consideration in most MRI experiments is how to reduce scanning time to improve patient comfort and reduce motion artifacts. In this work, we ease the problem by presenting an effective and lightweight model that supports fast training and accurate SR inference. The proposed network is inspired by the lateral inhibition mechanism, which assumes that there exist inhibitory effects between adjacent neurons. The backbone of our network consists of several lateral inhibition blocks, where the inhibitory effect is explicitly implemented by a battery of cascaded local inhibition units. When model scale is small, explicitly inhibiting feature activations is expected to further explore model representational capacity. For more effective feature extraction, several parallel dilated convolutions are also used to extract shallow features directly from the input image. Extensive experiments on various MR images (PD, T1 and T2 images) demonstrate that our lateral inhibition network (LIN) achieves better SR performance than other lightweight models with similar model scale.

Keywords: Convolutional neural network · lateral inhibition · magnetic resonance imaging · super-resolution.

1 Introduction

Magnetic resonance imaging (MRI) is an important and widely-used non-invasive medical imaging method with the advantage of multi-contrast and none ionizing radiation. Spatial resolution is one of the most important imaging parameters in most MRI scans. High-resolution (HR) images provide rich structural details and benefit accurate image post-processing, thus facilitating more effective early clinic diagnosis [28]. However, the resolution of magnetic resonance (MR) images is usually affected by various physical and physiological factors, such as hardware device, imaging time, signal-to-noise ratio (SNR), artifacts etc [28,27].

Image super-resolution (SR) provides an effective alternative to enhance the resolution of MR images from the perspective of post-processing [43], which aims
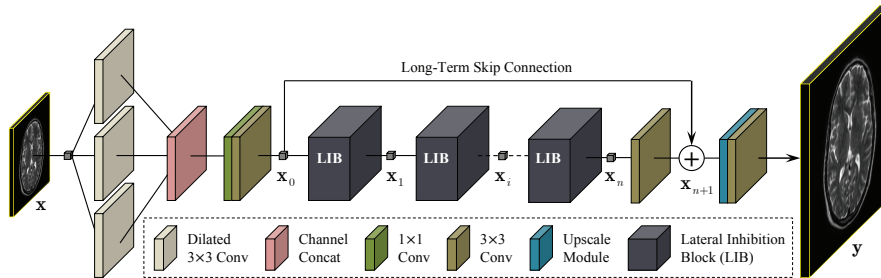
Fig. 1. The overall structure of our lateral inhibition network (LIN). The dilated 3×3 convolutions for feature extraction have different dilation rates to collect image features in the receptive fields with different sizes.

at recovering a HR image from one or more low-resolution (LR) images. As a post-processing method, image super-resolution is an active research field that can substantially breaks through the limitations of hardware device and improve image resolution [24,27]. In recent years, deep learning [16] technique, especially convolutional neural network (CNN) [17], has greatly promoted the development of this field, resulting in the emergence of many advanced SR models, such as SRCNN [4], DRCN [14], DRRN [35], MemNet [36], VDSR [13], EDSR [19], RDN [39], RCAN [38] etc. Although these models have excellent SR performance, they are mainly aimed at SR tasks of natural images, instead of MR images.

In medical image processing community, there are also some deep CNN-based medical image SR models, e.g., [26], [3], [2], [40], [43] etc. The primary intention of these models, to some extent, is to improve the performance of MR image SR tasks. However, a fundamental consideration in many MRI experiments is how to reduce imaging time to improve patient comfort and avoid motion artifacts as much as possible. Therefore, high-efficiency HR image reconstruction is also of significance in practical applications. On the other hand, an important problem in medical image processing with deep learning techniques is the degradation of training samples [20,43]. As the model scale (e.g., model parameters, network depth/width etc.) increases, it will be more difficult to train larger models with these degraded medical training samples [43,42], and more tricks are needed for successful model training [18]. In this regard, lightweight models *may* be more appropriate for medical image SR tasks.

With these considerations, we introduce a lightweight SR model to deal with single MR image SR tasks in this work. The proposed network is well-motivated by the lateral inhibition mechanism, which assumes that there exists inhibitory regulation between adjacent neurons. The building module of it is termed as local inhibition unit (LIU), which takes the residual block [19,39,38] as the backbone and a inhibition tail (IT) is attached to integrate the lateral inhibition mechanism into feature mapping. Generally, CNNs are built upon the convolution operation that extracts informative features by fusing spatial and channel-wise information together within local receptive fields. A great deal of work has shown that careful structural design favors to substantially improve the representational capacity of deep models [34,7,8,10,9,41]. The proposed LIU follows this point and serves as
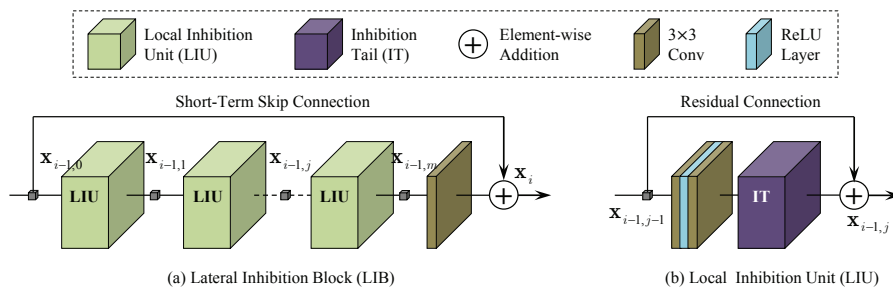
Fig. 2. The internal structure of the building modules of our LIN network. (a) The lateral inhibition block (LIB) consists of a series of local inhibition units (LIU) followed by a 3×3 conv layer. (b) A LIU contains two 3×3 conv layers with a ReLU layer [23] in the middle, followed by a inhibition tail (IT) that performs inhibitory regulation.

a feature regulator that simulates the Hartline-Rattliff equation and explicitly adjusts hierarchical features. This explicit adjustment of intermediate features is considered to help ease the representational burden of deep models and thus improve SR performance [9,43]. To extract more effective features and promote nonlinear mapping, we also adopt a set of parallel 3×3 dilated convolutions with different dilation rates to collect shallow features within the receptive fields with different sizes, as shown in Fig.1. Extensive experiments on various MR images show that our model achieves competitive SR performance with much less model parameters and higher efficiency.

2   Related Work

2.1   MR Image Super-Resolution

High-resolution medical images provide rich structural details that are critical for accurate image post-processing and early diagnoses. However, HR acquisition usually decreases SNR and increases scanning time [31,3]. As an alternate, image SR technique is widely used to enhance the resolution of MR images, and many SR methods for MR images are studied and proposed in the past decades, such as [25], [6], [33] that apply traditional multi-image super-resolution (MISR) to deal with MR image SR tasks, and [29], [21], [30] that focus on *single* medical image SR tasks, and the more advanced methods [26], [3], [43] and [42] etc. that are built upon deep CNNs. Due to unreasonable assumptions or models with limited representational capacity, the performance of early methods for medical image SR tasks is usually inferior and unsatisfactory. While some CNN-based methods achieve excellent performance, their models are large in scale and unfriendly to MRI with limited resources, e.g., [43] and [42].

2.2   Lightweight SR Models

After the pioneering work presented by Dong *et al.* [4], the CNN-based SR models show the mainstream trend of building deeper and larger networks for better SR
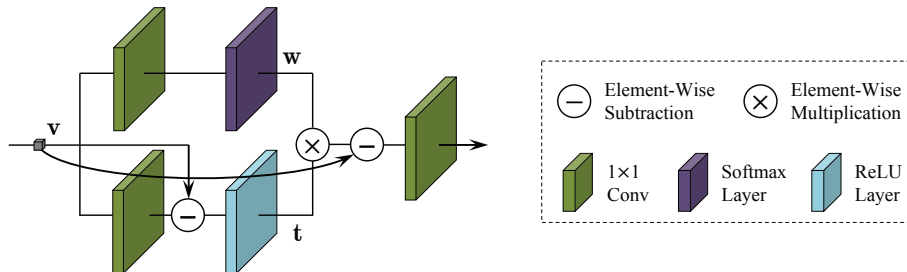
Fig. 3. The computing schema of a inhibition tail (IT). The upper branch imitates the weight tensor **w** of the Hartline-Ratliff equation, and the lower branch simulates its threshold tensor **t**. This part structure within a LIU acts as an inhibitory regulator of intermediate features.

Table 1. Ablation study on the components of the network structure. The maximum is marked in red and the second one is marked in blue (PSNR (dB) / SSIM).

FE	×	√	×	√
IT	×	×	√	√
$\mathcal{T}$(PD, BD) ×2	40.75 / 0.9880	40.81 / 0.9882	40.78 / 0.9881	40.84 / 0.9883

performance. Two representative large-scale models are MDSR [19] and RCAN [38], with network depths of over 160 and 400 layers respectively. A large number of model parameters and computing operations of large-scale SR models limit their practical applications. Some lightweight models have thus emerged, such as VDSR [13], IDN [11], CARN [1] and AWSRN [37] etc. Also, there are some lightweight SR models specializing in MR image SR tasks, e.g., RecNet [12] and FSCWRN [32]. All these methods suggest that lightweight models can achieve better trade-off between model performance and scale. In this work, we further improve this trade-off for single MR image SR tasks, by introducing a lightweight model that is motivated by lateral inhibition mechanism. We term it as lateral inhibition network (LIN).

3 Lateral Inhibition Network

3.1 Motivation: Visual Inhibition

In neurobiology, lateral inhibition is the capacity of an excited neuron to reduce the activity of its neighbors, which creates a contrast in stimulation that allows increased sensory perception. It occurs primarily in visual processes and is also referred to as lateral antagonism. A well-known model for simulating this visual inhibition is the Hartline-Ratliff equation:

$$\hat{v}_i = v_i - \sum_{j \neq i} w_{i,j} \cdot \max\left(0; v_j - t_{i,j}\right) \tag{1}$$

where $\hat{v}_i$ is the i-th element of the adjusted feature map $\hat{\mathbf{v}}$, v_i is the i-th element of the input feature map $\mathbf{v}$. $w_{i,j}$ is the inhibition coefficient of the j-th neuron on the

Table 2. Efficiency of the compared models. The sizes of 3D inputs for $r = 2$, $r = 3$ and $r = 4$ are $120 \times 120 \times 96$, $80 \times 80 \times 96$ and $60 \times 60 \times 96$ (seconds/volume).

scale	Bicubic [2D]	NLM [22]	SRCNN [4]	VDSR [13]	RecNet [12]	FSCWRN [32]	LIN [Ours]
$r = 2$	0.1543	90.4238	0.3021	1.7644	0.8231	2.1906	0.8501
$r = 3$	0.1578	63.5357	0.3211	2.6488	0.9652	1.1403	0.9689
$r = 4$	0.1610	46.0358	0.3284	2.4131	1.0277	0.7477	1.0788

i-th neuron, and $t_{i,j}$ represents the threshold that the j-th neuron must reach to inhibit the i-th neuron. As mentioned earlier, this explicit regulation of features is considered to help ease the representational burden of the model and thus improve the model performance. It is worth noting that Eqn.1 requires a nonlocal weighting, resulting in a substantial increase in computing effort. We simplified it by simply replace the nonlocal computation with ordinary convolutions.

3.2   Overall Network Structure

The overall structure of the proposed model is outlined in Fig.1 and Fig.2. The feature extraction is composed of a set of parallel dilated 3×3 convolutions, and a 1×1 convolution followed by a 3×3 convolution. The results of these dilation convolutions are concatenated together along the channel direction. This process can be formally represented as:

$$\mathbf{x}_0 = \mathcal{F}_{\text{ext}}(\mathbf{x}), \tag{2}$$

where $\mathbf{x}_0$ is the extracted shallow feature and $\mathbf{x}$ is the input image. $\mathcal{F}_{\text{ext}}(\cdot)$ implies the function corresponding to the entire feature extraction process. Next, $\mathbf{x}_0$ is fed into a series of cascaded lateral inhibition blocks (LIBs), which constitute the nonlinear mapping process:

$$\mathbf{x}_n = \mathcal{F}_b^n(\mathbf{x}_{n-1}) = \mathcal{F}_b^n(\mathcal{F}_b^{n-1}(\cdots \mathcal{F}_b^1(\mathbf{x}_0) \cdots)), \tag{3}$$

where $\mathbf{x}_i$ is the output of the i-th LIB, and the input of the $(i+1)$-th LIB. The function $\mathcal{F}_b^i(\cdot)$ corresponds to the mapping process of the i-th LIB. n is the total number of LIBs in the network. Finally, a 3×3 convolution is used to collect deep features and a long-term skip connection is used to conduct residual learning:

$$\mathbf{x}_{n+1} = \mathcal{T}(\mathbf{x}_n) + \mathbf{x}_0, \tag{4}$$

where $\mathbf{x}_{n+1}$ indicates the collected deep feature and $\mathcal{T}(\cdot)$ corresponds to the 3×3 convolution after $\mathbf{x}_n$, as shown in Fig.1. The image reconstruction part of our LIN consists of a upscale module followed by a 3×3 convolution, which is the same as EDSR [19].

3.3   Lateral Inhibition Block

The structure of LIB and LIU is shown in Fig.2. Let $\mathbf{x}_{i-1,0} = \mathbf{x}_{i-1}$ be the input of the i-th LIB and the first LIU in this LIB. The mapping process of a LIB can also be iteratively represented as:

$$\mathbf{x}_{i-1,m} = \mathcal{F}_u^m(\mathbf{x}_{i-1,m-1}) = \mathcal{F}_u^m(\mathcal{F}_u^{m-1}(\cdots \mathcal{F}_u^1(\mathbf{x}_{i-1,0}) \cdots)), \tag{5}$$

where m denotes the number of LIUs in each LIB, and the function $\mathcal{F}_u^j(\cdot)$ is the mapping process of the j-th LIU. Finally, a $3{\times}3$ conv layer is used to produce the final output of the i-th LIB, i.e., $\mathbf{x}_i$, as shown in Fig.2(a). The process can be formalized as:

$$\mathbf{x}_i = \mathcal{R}(\mathbf{x}_{i-1,m}) + \mathbf{x}_{i-1,0} = \mathcal{R}(\mathbf{x}_{i-1,m}) + \mathbf{x}_{i-1}, \qquad (6)$$

where $\mathcal{R}(\cdot)$ is the mapping process of the conv layer at the end. The lateral inhibition mechanism is explicitly implemented by the IT, which we will illustrate in subsection 3.4.

3.4   Inhibition Tail

The computing schema of the IT is shown in Fig.3. The upper branch simulates the weight $\mathbf{w}$ of Eqn.1, and the lower branch calculates the threshold $\mathbf{t}$. For the lower branch,

$$\mathbf{t} = \max\Big(0; \mathbf{v} - \mathcal{F}_t(\mathbf{v})\Big), \qquad (7)$$

where $\mathbf{t}$ is the weight tensor, and $\mathcal{F}_t(\cdot)$ denotes the $1{\times}1$ convolution in the lower branch of the Fig.2. For the upper branch,

$$\mathbf{w} = \sigma\Big(\mathcal{F}_w(\mathbf{v})\Big), \qquad (8)$$

where $\sigma(\cdot)$ is a softmax function, and $\mathcal{F}_w(\cdot)$ corresponds to the $1{\times}1$ convolution in the upper branch. Finally, the adjusted result can be obtained by:

$$\hat{\mathbf{v}} = \mathcal{F}(\mathbf{v} - \mathbf{w} \otimes \mathbf{t}), \qquad (9)$$

where $\otimes$ denotes element-wise multiplication and $\mathcal{F}(\cdot)$ represents the last $1{\times}1$ convolution in Fig.3. As can be seen, we use ordinary convolution operations to replace nonlocal weighting, to avoid heavy computation.

4   Experiments

4.1   Dataset

The dataset used in this study is the same as that used in [43]. It is derived from the IXI dataset[1] and contains 3 image types: PD, T1 and T2. For each MR image type, there are 500, 70 and 6 volumes of size $240{\times}240{\times}96$ (height$\times$width$\times$depth) for training, testing and validation, respectively. Besides, two image degradations are also included in the dataset, namely, bicubic downsampling (BD) and k-space truncation (TD). For the sake of convenience, we follow the convention descried in [43] to indicate each subset. For instance, $\mathcal{D}(\mathrm{PD, BD})$ implies the PD training set under bicubic downsampling, while $\mathcal{V}(\mathrm{T1, TD})$ represents the T1 validation set under k-space truncation degradation.

---

[1] http://brain-development.org/ixi-dataset/.

Table 3. Quantitative comparison between several typical SR models. The maximum values in each comparative cell are marked in red and the second ones are marked in blue. Both degradations (BD and TD) are included here. r is scaling factor and $\#\ P$ denotes the number of model parameters (PSNR (dB) / SSIM).

	Methods	r	$\#\ P$	PD	T1	T2
BD	Bicubic [2D]	×2	/	35.04 / 0.9664	33.80 / 0.9525	33.44 / 0.9589
	NLM [22]	×2	/	37.26 / 0.9773	35.80 / 0.9685	35.58 / 0.9722
	SRCNN [4]	×2	24.5K	38.96 / 0.9836	37.12 / 0.9761	37.32 / 0.9796
	VDSR [13]	×2	0.67M	39.97 / 0.9861	37.67 / 0.9783	38.65 / 0.9836
	RecNet [12]	×2	1.33M	40.43 / 0.9873	37.86 / 0.9792	39.13 / 0.9848
	FSCWRN [32]	×2	3.50M	40.72 / 0.9880	37.98 / 0.9797	39.44 / 0.9855
	LIN [Ours]	×2	1.33M	40.84 / 0.9883	38.04 / 0.9798	39.50 / 0.9857
	Bicubic [2D]	×3	/	31.20 / 0.9230	30.15 / 0.8900	29.80 / 0.9093
	NLM [22]	×3	/	32.81 / 0.9436	31.74 / 0.9216	31.28 / 0.9330
	SRCNN [4]	×3	24.5K	33.60 / 0.9516	32.17 / 0.9276	32.20 / 0.9440
	VDSR [13]	×3	0.67M	34.66 / 0.9599	32.91 / 0.9378	33.47 / 0.9559
	RecNet [12]	×3	1.33M	34.96 / 0.9623	33.05 / 0.9399	33.85 / 0.9588
	FSCWRN [32]	×3	3.50M	35.37 / 0.9653	33.24 / 0.9423	34.27 / 0.9618
	LIN [Ours]	×3	1.37M	35.39 / 0.9654	33.23 / 0.9421	34.26 / 0.9616
	Bicubic [2D]	×4	/	29.13 / 0.8799	28.28 / 0.8312	27.86 / 0.8611
	NLM [22]	×4	/	30.27 / 0.9044	29.31 / 0.8655	28.85 / 0.8875
	SRCNN [4]	×4	24.5K	31.10 / 0.9181	29.90 / 0.8796	29.69 / 0.9052
	VDSR [13]	×4	0.67M	32.09 / 0.9311	30.57 / 0.8932	30.79 / 0.9240
	RecNet [12]	×4	1.33M	32.58 / 0.9378	30.86 / 0.9005	31.30 / 0.9310
	FSCWRN [32]	×4	3.50M	32.91 / 0.9415	30.96 / 0.9022	31.71 / 0.9359
	LIN [Ours]	×4	1.36M	32.94 / 0.9417	31.01 / 0.9033	31.72 / 0.9361
TD	Bicubic [2D]	×2	/	34.65 / 0.9625	33.38 / 0.9460	33.06 / 0.9541
	NLM [22]	×2	/	36.18 / 0.9707	34.71 / 0.9581	34.56 / 0.9641
	SRCNN [4]	×2	24.5K	38.23 / 0.9802	36.52 / 0.9705	37.04 / 0.9773
	VDSR [13]	×2	0.67M	39.89 / 0.9850	37.58 / 0.9760	38.74 / 0.9823
	RecNet [12]	×2	1.33M	40.10 / 0.9857	37.54 / 0.9764	39.03 / 0.9832
	FSCWRN [32]	×2	3.50M	40.91 / 0.9876	38.04 / 0.9786	39.82 / 0.9851
	LIN [Ours]	×2	1.33M	41.11 / 0.9880	38.21 / 0.9793	40.02 / 0.9855
	Bicubic [2D]	×3	/	30.88 / 0.9167	29.79 / 0.8793	29.50 / 0.9016
	NLM [22]	×3	/	32.02 / 0.9324	30.83 / 0.9027	30.57 / 0.9197
	SRCNN [4]	×3	24.5K	32.90 / 0.9432	31.72 / 0.9187	31.80 / 0.9381
	VDSR [13]	×3	0.67M	34.27 / 0.9555	32.57 / 0.9304	33.23 / 0.9515
	RecNet [12]	×3	1.33M	34.67 / 0.9590	32.80 / 0.9347	33.69 / 0.9554
	FSCWRN [32]	×3	3.50M	35.30 / 0.9636	33.09 / 0.9390	34.34 / 0.9603
	LIN [Ours]	×3	1.37M	35.39 / 0.9642	33.25 / 0.9406	34.45 / 0.9609
	Bicubic [2D]	×4	/	28.82 / 0.8713	27.96 / 0.8182	27.60 / 0.8511
	NLM [22]	×4	/	29.27 / 0.8906	28.68 / 0.8439	28.37 / 0.8718
	SRCNN [4]	×4	24.5K	30.52 / 0.9078	29.31 / 0.8616	29.32 / 0.8960
	VDSR [13]	×4	0.67M	31.69 / 0.9244	30.14 / 0.8818	30.51 / 0.9162
	RecNet [12]	×4	1.33M	32.16 / 0.9310	30.46 / 0.8900	31.03 / 0.9243
	FSCWRN [32]	×4	3.50M	32.78 / 0.9387	30.79 / 0.8973	31.71 / 0.9334
	LIN [Ours]	×4	1.36M	32.82 / 0.9391	30.88 / 0.8990	31.77 / 0.9339

| Bicubic | NLM [22] | SRCNN [4] | VDSR [13] | RecNet [12] | FSCWRN [32] | LIN [**Ours**] | Ground Truth |

29.61 / 0.8254   30.64 / 0.8622   31.30 / 0.8793   31.95 / 0.8942   32.21 / 0.9010   **32.33 / 0.9030**   **32.37 / 0.9042**   PSNR / SSIM

28.38 / 0.8811   29.48 / 0.9064   30.56 / 0.9242   31.91 / 0.9427   32.63 / 0.9497   **33.15 / 0.9543**   **33.19 / 0.9545**   PSNR / SSIM
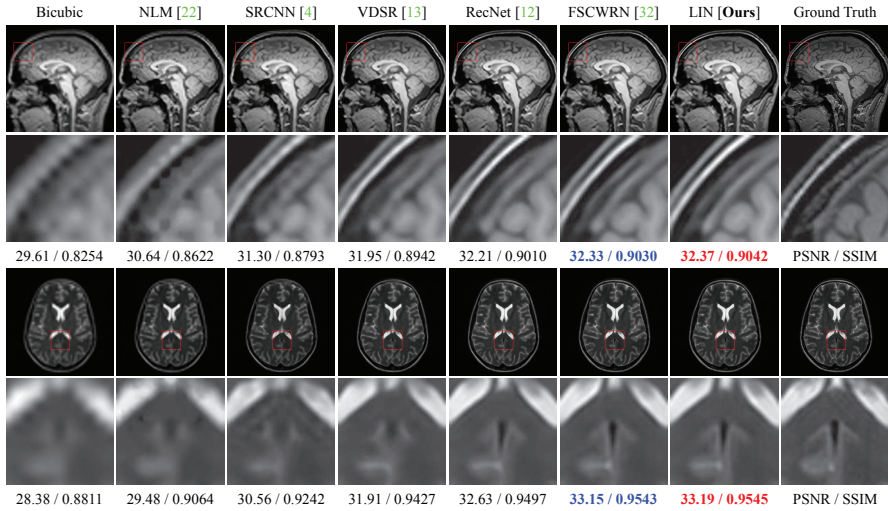
Fig. 4. The visual comparison of several typical lightweight SR models on a T1 image (top) and a T2 image (bottom) with $r = 4$ and **BD** degradation.

4.2   Implementation Details

We set $n = m = 4$ for our finalized model. The number of channels for the two conv layers in each LIU is 128 and 32 respectively. Elsewhere, it is 32 except for the final output layer. Batch size is set to be 16. The models are trained with LR image patches of size 24×24 randomly extracted from 2D MR slices with the corresponding HR patches. The training data is augmented by random horizontal flips and 90° rotations. All models are implemented in TensorFlow 1.9.0 and trained on a NVIDIA GeForce GTX 1080 Ti GPU for 10^6 iterations. We use Xavier's method [5] to initialize all model parameters and Adam optimizer [15] to minimize the loss by setting $\beta_1 = 0.9$, $\beta_2 = 0.999$ and $\epsilon = 10^{-8}$. Learning rate is initialized as 2×10^{-4} for all layers and halved at every 2×10^5 iterations.

4.3   Model Analysis

In this section, we study the impact of the structural components of the model on the SR performance, including feature extraction (FE) and the inhibition tail (IT). In Table 1, the comparative case for FE is to replace the parallel dilated conv layers ($\sqrt{}$) with a single 3×3 conv layer ($\times$). As for IT, "$\times$" means simply removing the component from the LIU. The evaluation is performed on the test set of PD images with scaling factor $r = 2$. As can be seen, the baseline structure without FE and IT gives the evaluation values of 40.75dB and 0.9880, and the performance can be improved by adding FE or IT. Besides, the co-occurrence of FE and IT within the network can further boost the performance.

These comparisons indicate that the proposed parallel feature extraction and the active inhibitory regulation of intermediate features contribute to improve the representational capacity and obtain better SR performance.
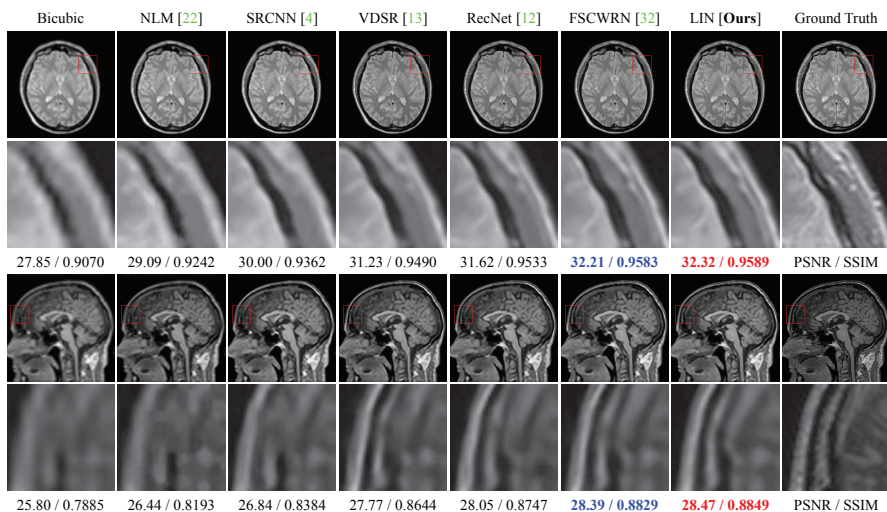
Bicubic	NLM [22]	SRCNN [4]	VDSR [13]	RecNet [12]	FSCWRN [32]	LIN [**Ours**]	Ground Truth
27.85 / 0.9070	29.09 / 0.9242	30.00 / 0.9362	31.23 / 0.9490	31.62 / 0.9533	**32.21 / 0.9583**	**32.32 / 0.9589**	PSNR / SSIM
25.80 / 0.7885	26.44 / 0.8193	26.84 / 0.8384	27.77 / 0.8644	28.05 / 0.8747	**28.39 / 0.8829**	**28.47 / 0.8849**	PSNR / SSIM

Fig. 5. The visual comparison on a PD image (top) and a T1 image (bottom) with $r = 3$ and $r = 4$, respectively. The image degradation is k-space truncation (**TD**).

4.4 Comparison with Other Methods

We illustrate the effectiveness of the proposed LIN model by comparing it with several typical SR methods, including: (1) the NLM [22] specifically for MRI upsampling; (2) SRCNN [4] and VDSR [13] for natural images; (3) RecNet [12] and FSCWRN [32] specifically for MR images. The quantitative results of these methods are directly cited from [42]. Note that we only compare the models that have roughly similar number of parameters as our LIN model.

Quantitative Evaluation Table 3 shows the quantitative comparison between these methods. Overall, as can be observed, our LIN model achieves the best SR performance although it has more moderate model parameters, almost the same as RecNet [12]. The network parameters of FSCWRN [32] are about 2.6 times that of ours, but our LIN model still performs better. In case of TD, our model moves beyond other methods in terms of all comparative cases. This may indicate that our LIN method is more suitable for MR image SR tasks, as the k-space truncation degradation aims to simulate the image acquisition process in real-world MRI [43].

Visual Comparison Fig.4 and Fig.5 show the visual comparison between these methods. Also, we can see that the proposed LIN model presents the best visual effect on various MR images. For instance, the bottom row of Fig.5 is the visual comparison on a T1 image with TD degradation and $r = 4$, the contour between the gray ridge and the dark groove is clearer in results of our model, presenting a clear indication of the ground truth.

Efficiency Table 2 shows the efficiency comparison between these methods. We collected the results with a Omnisky supercomputing workstation equipped with

64GB memory and two Intel Xeon E5-2630 CPUs (2.20 GHz). The CNN-based methods are evaluated with a single NVIDIA GTX 1080 Ti GPU. The running time is averaged on on a 3D volume instead of a 2D slices, as medical images are usually organized as 3D volumes. We can see from Table. 2 that our LIN model can reconstruct HR volumes in about 1s, for all scaling factors. This implies that our model is not only highly accurate in SR performance, but also practically useful in real-world applications.

5   Conclusion

We present a lightweight CNN model for MR image SR tasks in this work, which is directly motivated by the visual inhibition mechanism. The inhibition tail in our model acts as a feature regulator that explicitly adjusts the activation of hidden neurons. When the model is small in scale, it is considered to help ease the representational burden of models and improve the SR performance. Extensive experiments on different MR images exhibit the superiority of our LIN model over other lightweight SR models. Because of the better tradeoff between model scale and performance, it is more suitable for real-world deployment.

References

1. Ahn, N., Kang, B., Sohn, K.: Fast, accurate, and lightweight super-resolution with cascading residual network. In: ECCV. pp. 256–272 (2018)
2. Chen, Y., Shi, F., Christodoulou, A.G., *et al.*: Efficient and accurate MRI super-resolution using a generative adversarial network and 3D multi-level densely connected network. In: MICCAI 2018. pp. 91–99 (2018)
3. Chen, Y., Xie, Y., Zhou, Z., *et al.*: Brain MRI super resolution using 3D deep densely connected neural networks. In: 15th IEEE International Symposium on Biomedical Imaging, ISBI 2018. pp. 739–742 (2018)
4. Dong, C., Loy, C.C., He, K., Tang, X.: Image super-resolution using deep convolutional networks. IEEE Trans. Pattern Anal. Mach. Intell. **38**(2), 295–307 (2016)
5. Glorot, X., Bengio, Y.: Understanding the difficulty of training deep feedforward neural networks. In: AISTATS 2010. pp. 249–256 (2010)
6. Greenspan, H., Peled, S., Oz, G., Kiryati, N.: MRI inter-slice reconstruction using super-resolution. In: MICCAI 2001. pp. 1204–1206 (2001)
7. He, K., Zhang, X., Ren, S., Sun, J.: Deep residual learning for image recognition. In: CVPR. pp. 770–778 (2016)
8. He, K., Zhang, X., Ren, S., Sun, J.: Identity mappings in deep residual networks. In: ECCV. pp. 630–645 (2016)
9. Hu, J., Shen, L., Albanie, S., Sun, G., Wu, E.: Squeeze-and-excitation networks. arXiv preprint **arxiv:1709.01507** (2017)
10. Huang, G., Liu, Z., *et al.*: Densely connected convolutional networks. In: CVPR. pp. 2261–2269 (2017)
11. Hui, Z., Wang, Xiumei Gao, X.: Fast and accurate single image super-resolution via information distillation network. arXiv preprint **arxiv:1803.09454** (2018)
12. Hyun, C.M., Kim, H.P., Lee, S.M., *et al.*: Deep learning for undersampled MRI reconstruction. arXiv preprint **arxiv:1709.02576** (2017)

13. Kim, J., Lee, J.K., Lee, K.M.: Accurate image super-resolution using very deep convolutional networks. In: CVPR 2016. pp. 1646–1654 (2016)
14. Kim, J., Lee, J.K., Lee, K.M.: Deeply-recursive convolutional network for image super-resolution. In: CVPR 2016. pp. 1637–1645 (2016)
15. Kingma, D.P., Ba, J.: Adam: A method for stochastic optimization. In: ICLR (2015)
16. LeCun, Y., Bengio, Y., Hinton, G.: Deep learning. Nature **521**(7553), 436–444 (2015)
17. LeCun, Y., Boser, B.E., *et al.*: Backpropagation applied to handwritten zip code recognition. Neural Computation **1**(4), 541–551 (1989)
18. Li, J., Fang, F., Mei, K., Zhang, G.: Multi-scale residual network for image super-resolution. In: ECCV. pp. 527–542 (2018)
19. Lim, B., Son, S., Kim, H., Nah, S., Lee, K.M.: Enhanced deep residual networks for single image super-resolution. In: CVPR Workshops 2017. pp. 1132–1140 (2017)
20. Litjens, G., Kooi, T., *et al.*: A survey on deep learning in medical image analysis. Medical Image Analysis **42**(9), 60–88 (2017)
21. Manjón, J.V., Coupé, P., Buades, A., Collins, D.L., Robles, M.: MRI superresolution using self-similarity and image priors. International Journal of Biomedical Imaging **2010**(Article ID 425891), 425891 (2010)
22. Manjón, J.V., Coupé, P., Buades, A., *et al.*: Non-local MRI upsampling. Medical Image Analysis **14**(6), 784–792 (2010)
23. Nair, V., Hinton, G.E.: Rectified linear units improve restricted boltzmann machines. In: ICML 2010. pp. 807–814 (2010)
24. Park, S.C., Min, K.P., Kang, M.G.: Super-resolution image reconstruction: a technical overview. IEEE Signal Processing Magazine **20**(3), 21–36 (2003)
25. Peled, S., Yeshurun, Y.: Super-resolution in MRI: application to human white matter fiber tract visualization by diffusion tensor imaging. Magnetic Resonance in Medicine **45**(1), 29–35 (2015)
26. Pham, C.H., Ducournau, A., Fablet, R., Rousseau, F.: Brain MRI super-resolution using deep 3D convolutional networks. In: 14th IEEE International Symposium on Biomedical Imaging, ISBI 2017. pp. 197–200 (2017)
27. Plenge, E., Poot, D.H.J., Bernsen, M., *et al.*: Super-resolution methods in MRI: can they improve the trade-off between resolution, signal-to-noise ratio, and acquisition time? Magnetic Resonance in Medicine **68**(6), 1983–1993 (2012)
28. Reeth, E.V., Tham, I.W., *et al.*: Super-resolution in magnetic resonance imaging: A review. Concepts in Magnetic Resonance Part A **40A**(6), 306–325 (2012)
29. Rousseau, F.: Brain hallucination. In: ECCV 2008. pp. 497–508 (2008)
30. Rueda, A., Malpica, N., Romero, E.: Single-image super-resolution of brain MR images using over complete dictionaries. Med. Imag. Analy. **17**(1), 113–132 (2013)
31. Shi, F., Cheng, J., Wang, L., Yap, P.T., Shen, D.: LRTV: MR image super-resolution with low-rank and total variation regularizations. IEEE Transactions on Medical Imaging **34**(12), 2459–2466 (2015)
32. Shi, J., Li, Z., Ying, S., *et al.*: MR image super-resolution via wide residual networks with fixed skip connection. IEEE Journal of Biomedical and Health Informatics **23**(3), 1129–1140 (2019)
33. Shilling, R.Z., Robbie, T.Q., *et al.*: A super-resolution framework for 3D high-resolution and high-contrast imaging using 2D multislice MRI. IEEE Trans. Med. Imaging **28**(5), 633–644 (2009)
34. Simonyan, K., Zisserman, A.: Very deep convolutional networks for large-scale image recognition. In: ICLR (2015)

35. Tai, Y., Yang, J., Liu, X.: Image super-resolution via deep recursive residual network. In: CVPR 2017. pp. 2790–2798 (2017)
36. Tai, Y., Yang, J., Liu, X., Xu, C.: MemNet: A persistent memory network for image restoration. In: ICCV 2017. pp. 4549–4557 (2017)
37. Wang, C., Li, Z., Shi, J.: Lightweight image super-resolution with adaptive weighted learning network. arXiv preprint **arxiv:1904.02358** (2019)
38. Zhang, Y., Li, K., Li, K., *et al.*: Image super-resolution using very deep residual channel attention networks. In: ECCV 2018. pp. 294–310 (2018)
39. Zhang, Y., Tian, Y., Kong, Y., Zhong, B., Fu, Y.: Residual dense network for image super-resolution. In: CVPR 2018. pp. 2472–2481 (2018)
40. Zhao, C., Carass, A., Dewey, B.E., Prince, J.L.: Self super-resolution for magnetic resonance images using deep networks. In: 15th IEEE International Symposium on Biomedical Imaging, ISBI 2018. pp. 365–368 (2018)
41. Zhao, L., Li, M., *et al.*: Deep convolutional neural networks with merge-and-run mappings. In: IJCAI. pp. 3170–3176 (2018)
42. Zhao, X., Zhang, H., Liu, H., Qin, Y., Zhang, T., Zou, X.: Single MR image super-resolution via channel splitting and serial fusion network. arXiv preprint **arxiv:1901.06484** (2019)
43. Zhao, X., Zhang, Y., Zhang, T., Zou, X.: Channel splitting network for single MR image super-resolution. arXiv preprint **arxiv:1810.06453** (2018)